Understanding cracking behavior of glass from its response to hydrostatic compression

Siva Priya Jaccani,[1] Randall E. Youngman,[2] John C. Mauro,[3] and Liping Huang[1,*]

[1]*Department of Materials Science and Engineering, Rensselaer Polytechnic Institute, Troy, New York 12180, USA*

[2]*Science and Technology Division, Corning Incorporated, Corning, New York 14831, USA*

[3]*Department of Materials Science and Engineering, The Pennsylvania State University, University Park, Pennsylvania 16802, USA*

(Received 20 December 2019; accepted 5 May 2020; published 25 June 2020)

Under sharp contact loading, glass deforms elastically and then plastically in the form of densification, shear flow, and network structure changes, which interplay with each other and lead to stress/residual stress buildup and cracking. Vickers indentation is often used to study the deformation and cracking behavior of glass; however, it is not easy to delineate the individual contribution of each deformation mode under indentation due to experimental difficulties associated with *in situ* investigations at a local scale (tens of microns) under nonuniform stresses. Given the stress field under an indenter is largely compressive, hydrostatic compression and decompression in a diamond anvil cell (DAC) were used in this work to help understand the response of glass to indentation during the loading and unloading process. To this end, an optical microscopy technique was developed to measure the volume of glass under pressure in the DAC by using argon as a pressure transmitting medium. This provided the densification and recovery of glass under hydrostatic compression and decompression. *In situ* Brillouin light scattering experiments were carried out at the same time to measure the elastic response of glass to pressure. A few multicomponent glasses with vastly different indentation cracking behaviors were selected for study in this work. Our experiments reveal that glass with a high ability to undergo reversible structure changes in response to hydrostatic compression and decompression shows a high cracking resistance under sharp contact loading.

DOI: 10.1103/PhysRevMaterials.4.063607

I. INTRODUCTION

Glasses have become ubiquitous in a wide range of high-tech applications, but the main challenge in their end use is their low resistance to damage in the form of cracks or scratches [1]. A variety of postprocessing techniques such as ion exchange and thermal tempering are employed to introduce surface compressive stresses to improve damage/crack resistance [2,3]. Recently, much attention has been drawn towards using composition and thermal history to optimize the damage resistance of glasses without the need for extensive postprocessing techniques [4–14]. Especially, B_2O_3-containing glasses have been extensively studied for their exceptional crack resistance [12–15]. Designing glasses with high damage resistance is critical for their applications, but the underlying cracking mechanisms are complex to understand and analyze. Before cracking under a sharp contact load, glasses undergo elastic and inelastic deformation with densification and shear flow being the main deformation mechanisms. Glasses with low Poisson's ratios tend to densify, whereas those with high Poisson's ratios tend to shear flow under indentation [16]. Apart from densification and shear flow, network adaptivity was recently proposed to be an additional deformation mechanism [6,17]. The interplay between these different deformation mechanisms leads to the buildup of stress and residual stress, and ultimately results in cracking. A fundamental understanding of crack initiation can help improve the performance of glass against contact cracking by optimizing the composition and thermal-history design.

Traditionally, Vickers indentation has been used to understand plastic deformation in glasses, but the stress state as well as the deformation mechanism under an indenter are extremely complex. In addition, there are several difficulties associated with experimental investigation at a local scale (tens of microns) with varying stress distribution under a Vickers indenter. Given that the stress field under an indenter is largely compressive, but very hard to quantify, cold-compression and hot-compression treatments were previously used to gain insights into the response of glass to high compressive loads [18,19]. Insight from pressure processing techniques was linked to glass deformation/cracking because stresses on the same order of magnitude develop in glasses under sharp contact loading [4–7,18]. However, in such experiments, observations were made *ex situ* after the compression treatment was completed [4–7]. *In situ* experiments that provide a more comprehensive picture of the response of glass to loading and unloading at room temperature are limited, motivating our efforts to close this gap and pave the way for a better understanding of glass cracking. In this work, we used Brillouin light scattering (BLS) and optical microscopy *in situ* in a diamond anvil cell (DAC) to study the elastic response of glass to pressure and the pressure dependence of volume [equation of state (EOS)] [20–25], respectively. EOS and elastic moduli of glasses under pressure will help us understand how the structure and properties of glass evolve under indentation [18]. In addition, they serve as critical inputs for developing force

*huangL5@rpi.edu

TABLE I. Physical properties of glasses studied in this work.

	Density (g/cm^3)	Hardness at 4.9 N (kgf/mm^2)	Poisson's ratio	Young's modulus (GPa)	Bulk modulus (GPa)	Shear modulus (GPa)
As-drawn 20% B_2O_3	2.231	518 (±21)	0.239 (±0.003)	56.3 (±0.4)	36.0 (±0.2)	22.7 (±0.2)
Annealed 20% B_2O_3	2.240	507 (±39)	0.237 (±0.001)	59.3 (±0.1)	37.5 (±0.1)	24.0 (±0.1)
10% B_2O_3	2.385	556 (±16)	0.236 (±0.002)	73.0 (±0.2)	46.2 (±0.2)	29.5 (±0.1)
0% B_2O_3	2.432	582 (±32)	0.212 (±0.001)	73.0 (±0.1)	42.3 (±0.1)	30.1 (±0.1)

fields with accurate short- and long-range interactions for molecular dynamics simulations of glasses [26], and for validating constitutive models in finite element analysis of glass mechanics [27].

In this work, a few multicomponent commercial glasses with vastly different indentation cracking behaviors were selected. *In situ* experiments conducted on these glasses revealed that a glass network with a high ability to undergo reversible structure changes in response to hydrostatic compression and decompression shows a high cracking resistance under sharp contact loading. It is of critical importance to develop a fundamental understanding of the factors that control crack resistance because this knowledge will facilitate the design of glasses with high damage resistance by tuning chemical composition, thermal history, and network structure in a controllable manner.

II. EXPERIMENTAL METHOD

Commercial multicomponent oxide glasses containing different B_2O_3 contents were chosen for this study [1,28,29]: 20% B_2O_3, 10% B_2O_3, and 0% B_2O_3. 20% B_2O_3 glass samples with different fictive temperatures were considered here because previous studies have shown that structure and properties of glasses containing a high content of boron are very sensitive to thermal history [12,13]. The 20% B_2O_3 sample with a higher fictive temperature, synthesized by the Corning fusion-draw process without annealing, is labeled "as-drawn 20% B_2O_3 glass" hereafter. The 20% B_2O_3 sample with a lower fictive temperature, obtained by annealing below the glass transition temperature (T_g) for 2 h, is referred to as "annealed 20% B_2O_3 glass." The 10% B_2O_3 and 0% B_2O_3 samples used for mechanical tests are as-drawn glasses synthesized by Corning's fusion-draw process without annealing.

A six-pass high-contrast Fabry-Perot interferometer from JSR Scientific Instruments was used for measuring Brillouin frequency shifts in this study. BLS experiments in the emulated platelet geometry (EPG) were carried out to measure both longitudinal (V_L) and transverse sound (V_T) velocities at room temperature for all samples. Details of the experimental setup, the light scattering geometry, and its applications can be found elsewhere [30–32]. From the sound velocities measured in BLS, together with the density (ρ), the longitudinal elastic modulus (C_{11}), Young's modulus (E), bulk modulus (K), shear modulus (C_{44} or μ), and the Poisson's ratio (ν) can be calculated using the following equations, and are presented in Table I.

$$C_{11} = \rho V_L^2, \tag{1}$$

$$C_{44} = \rho V_T^2, \tag{2}$$

$$E = C_{44}\frac{3C_{11} - 4C_{44}}{C_{11} - C_{44}}, \tag{3}$$

$$K = \frac{3C_{11} - 4C_{44}}{3}, \tag{4}$$

$$\mu = C_{44}, \tag{5}$$

$$\nu = \frac{E}{2\mu} - 1. \tag{6}$$

A membrane-driven diamond anvil cell (DAC) was used to generate hydrostatic stress states. Optically polished glass samples (~100 μm × 100 μm × 10–20 μm in size), a ruby ball (5–10 μm in diameter) as a pressure calibrant [33], and argon as a pressure transmitting medium [34] (PTM) were loaded into a hole drilled in a stainless-steel gasket. The PTM was loaded into the DAC cryogenically [19]. *In situ* BLS experiments were conducted to measure the longitudinal Brillouin frequency shift of glass as a function of pressure. BLS measurements were taken through the diamond anvil of the DAC in the backscattering geometry. Longitudinal Brillouin frequency shift (Δf_L) measured in the backscattering geometry is related to V_L as

$$V_L = \frac{\lambda_0 \Delta f_L}{2n}, \tag{7}$$

where n is the refractive index and λ_0 is the laser wavelength [30]. A Horiba LabRAM HR800 Raman spectrometer was used to measure the pressure-dependent ruby fluorescence shift to calculate the hydrostatic pressure in the DAC [35]. A 532-nm Verdi V2 DPSS green laser was used as the probing light source for both BLS and ruby fluorescence measurements. A Dino-Lite microscope combined with a 20× long working distance objective lens was set up to view the sample in the DAC as seen in Fig. 1 (left). This optical microscopy setup allows us to measure the sample area and identify spots for BLS experiments under pressure. The same magnification was maintained throughout the experiment. A typical micrograph generated from the DAC is shown in Fig. 1 (right). The sample area was estimated by counting pixels in the digital image using the GWYDDION program [36]. To

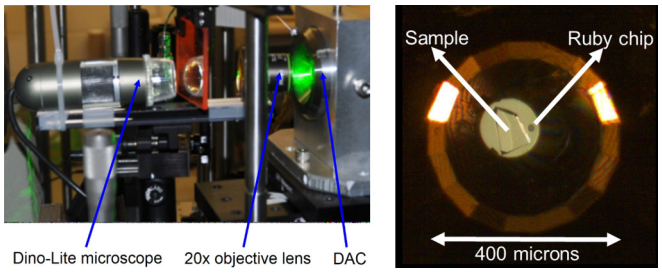

FIG. 1. (Left) Optical microscopy setup for EOS measurements and for viewing sample during BLS experiments in a DAC. (Right) Optical micrograph showing a glass sample and a ruby ball under pressure in a DAC.

determine the EOS, isotropic compression was assumed to calculate the sample volume under pressure from the sample area: $\frac{V_P}{V_0} = (\frac{A_P}{A_0})^{3/2}$, where V_0 and A_0 are the volume and area under ambient conditions, respectively; V_P and A_P are the corresponding ones under pressure in the DAC [20,37]. Uncertainty in $\frac{V_P}{V_0}$ estimations is expected to be $\pm$ 0.003. After a certain pressure was reached in the DAC, the sample was equilibrated for 15–20 min [19,38] before any optical micrograph or BLS spectrum was collected (pressure measured from ruby fluorescence was found to stabilize in around 15 min). BLS spectrum collection time is ~6–10 min at each pressure.

The advantages of using this optical microscopy setup together with a membrane-driven DAC are that EOS and BLS measurements under pressure can be collected simultaneously and the ruby fluorescence can be measured *in situ* without moving the DAC after each pressure increment. This will guarantee that the same spot is measured under different pressures.

Optical microscopy has been used for measuring EOS owing to its simplicity, but the technique was previously limited in its implementation to pressures below 10 GPa [20,24,39]. In this work, we successfully extended this technique for EOS measurements to pressures up to 19 GPa by using a pixel-dense Dino-Lite microscope camera and reliable image processing software such as the GWYDDION program [36]. A standard high-purity silica glass, Corning 7980 fused silica, was used to test the reliability of our setup. Figure 2 shows excellent agreement between the EOS of silica glass measured in our study compared to a previous work in the literature [20], proving the feasibility of this experimental setup.

Vickers hardness (H_V) of all glass samples in this study was calculated from image analysis of Vickers indents made at 0.5 kgf (4.9 N) load according to

$$H_V = \frac{2P \sin\left(\frac{\alpha}{2}\right)}{d^2}, \tag{8}$$

where P is the Vickers load, α is the angle between indenter faces, and d is the mean diagonal length of the indent. Results presented in Table I are Vickers hardness values averaged from at least ten indents.

To calculate the crack initiation load, Vickers indents were made at incremental loads of 0.49, 0.98, 1.96, 2.94, 4.9, and 9.8 N. Crack probability is determined by counting the number of cracks emanating from the corners of the indent

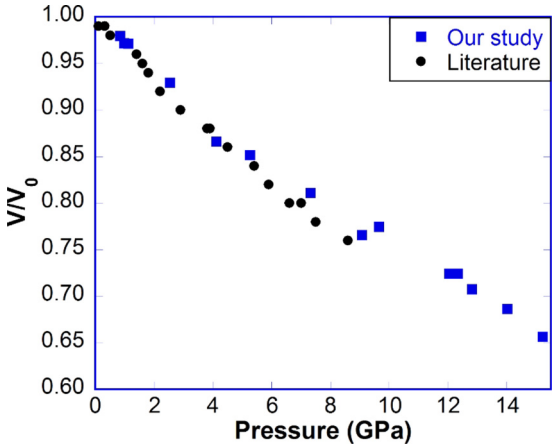

FIG. 2. EOS of silica glass measured by the optical microscopy technique in our study in comparison with data from the literature [20].

at systematically increasing indentation loads. An average of data from at least ten Vickers indents was obtained to estimate the number of cracks at each load.

To understand the contribution of densification and shear flow during Vickers indentation, atomic force microscopy (AFM) was used to profile Vickers indents immediately after indentation and postannealing at $0.9T_g$ (in K) for 1 h. At least eight indents of 0.98 N load were used for analysis with the help of the GWYDDION program [36]. By following the procedure established by Yoshida *et al.* [40], the volumes of permanent deformation affected by densification (V_d) and shear flow (V_s) can be calculated.

^{11}B magic-angle spinning (MAS) nuclear magnetic resonance (NMR) experiments were conducted to understand the coordination environment of boron in boron-containing glasses [7].

III. RESULTS AND DISCUSSION

A. Glass structure, crack resistance, and deformation modes of glasses under indentation

Figure 3 presents ^{11}B MAS NMR results from our samples; the peak towards the left in the spectrum corresponds to the trigonal boron resonance and that on the right corresponds to the tetrahedral boron resonance. The NMR data show that boron is primarily in the trigonal coordination state, but there is a small fraction of tetrahedral coordinated boron that increases as the boron content in the glasses increases or after annealing. As-drawn and annealed glass with 20% B_2O_3 have different contents of fourfold coordinated boron (3.7% and 6.5%, respectively), whereas the coordination of boron in the 10% B_2O_3 samples is not sensitive to the change in thermal history (3.1% fourfold coordinated boron).

The trigonal boron resonances (peak between 0 and 15 ppm) comprise two peaks, generally attributed to ring and nonring BO_3 units. This trigonal boron resonance peak visibly changes after annealing for the 20% B_2O_3 glass as seen in the ^{11}B MAS NMR spectrum in Fig. 3(a) which implies that changes in the intermediate-range order (IRO) also occur with

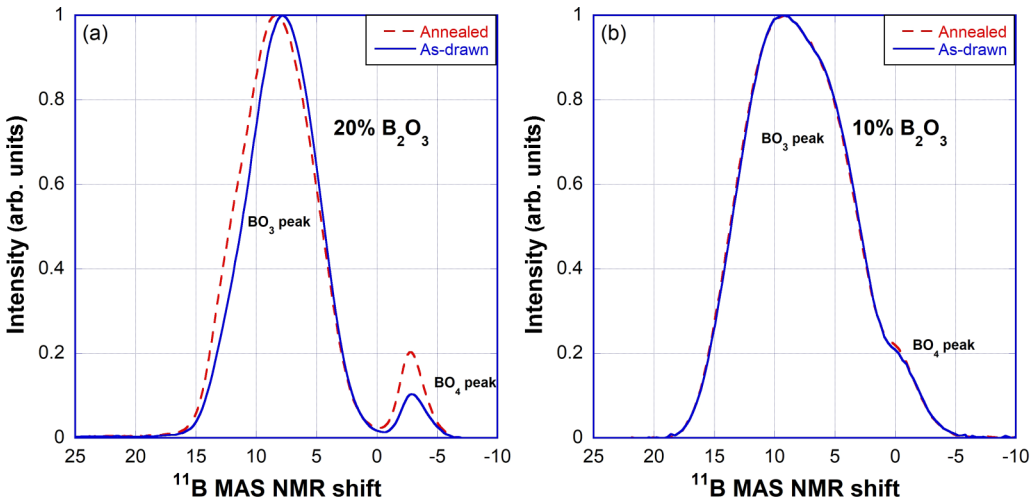

FIG. 3. ^{11}B MAS NMR spectra of as-drawn and annealed (for 2 h near T_g) (a) 20% and (b) 10% B_2O_3 glasses. Note: The overlapping of the BO_4 peak with the BO_3 peaks in (b) is due to a lower external magnetic field applied for NMR measurements [16.4 T vs 11.7 T in (a), (b), respectively].

thermal history along with changes in the short-range order (SRO).

Vickers indentation was performed on these glass samples at incremental loads and typical optical micrographs of the Vickers indents generated at 9.8 N are shown in Fig. 4.

The crack probability plotted as a function of indentation load for these samples is shown in Fig. 5. The highest possible load that our Vickers indenter can achieve is 9.8 N. Sigmoidal function forms were fit to the experimental data. Crack initiation load, defined as the load at which the crack probability is 50%, is the highest for the as-drawn 20% B_2O_3 sample, followed by annealed 20% B_2O_3, then 10% B_2O_3, and is the least for 0% B_2O_3 glass as seen in Fig. 5.

It has generally been observed that high crack resistance does not correlate with fracture toughness or hardness [10,41,42]. The ratio of hardness to fracture toughness, previously defined as the brittleness [43], was also found to not be correlated with crack resistance [42,44]. Previous studies on glassy solids found good correlations between Poisson's ratio and intrinsic ductility or brittleness [45,46]. For the glasses considered here, Poisson's ratio values are quite close as seen in Table I, yet the crack initiation loads were found to be very different. This shows that Poisson's ratio may not be a good indicator of crack resistance under indentation, probably because of the complex nature of the stress field underneath the indent.

Yoffe described the stress around an indent by superposing the Boussinesq field originating from a point load normal to the surface of a semi-infinite elastic body, and a blister field

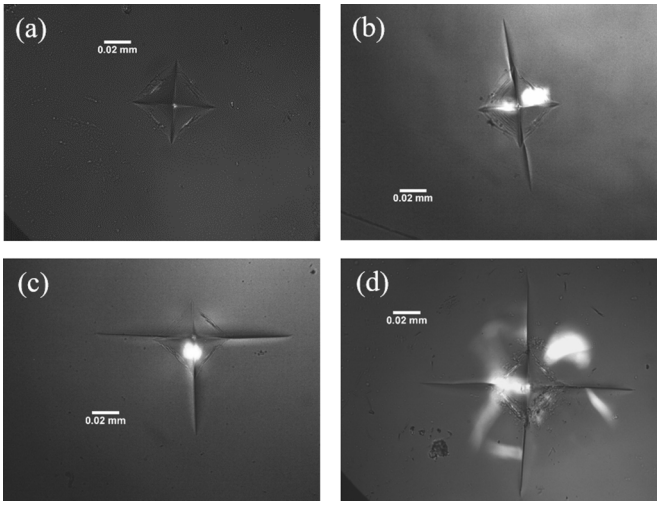

FIG. 4. Optical micrograph of Vickers indent in (a) as-drawn 20% B_2O_3, (b) annealed 20% B_2O_3, (c) 10% B_2O_3, and (d) 0% B_2O_3 glasses made at 9.8 N load in air.

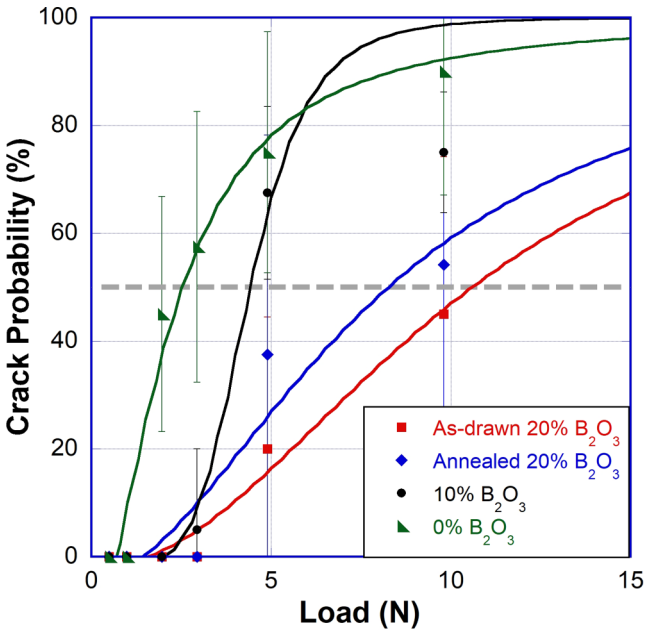

FIG. 5. Crack probability as a function of the Vickers indentation load. The horizontal dashed line indicates the 50% crack probability.

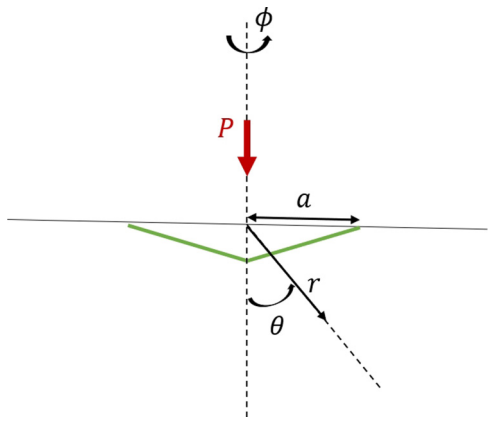

FIG. 6. A schematic of the spherical coordinate system for the stress field around an indent.

arising from the strain nucleus, created by the yield zone under the indenter [47] according to

$$\sigma_{rr} = \frac{P}{2\pi r^2}[1 - 2\nu - 2(2-\nu)\cos^2\theta] + \frac{4B}{r^3}[(5-\nu)\cos^2\theta - (2-\nu)], \quad (9)$$

$$\sigma_{\theta\theta} = \frac{P}{2\pi r^2}\frac{(1-2\nu)\cos\theta}{(2+\cos\theta)} - \frac{2B}{r^3}(1-2\nu)\cos^2\theta, \quad (10)$$

$$\sigma_{\phi\phi} = \frac{P}{2\pi r^2}(1-2\nu)\left(\cos\theta - \frac{1}{1+\cos\theta}\right) - \frac{2B}{r^3}(2-3\cos^2\theta), \quad (11)$$

$$\sigma_{r\theta} = \frac{P}{2\pi r^2}\left[\frac{(1-2\nu)\sin\theta\cos\theta}{1+\cos\theta}\right] + \frac{4B}{r^3}(1+\nu)\sin\theta\cos\theta, \quad (12)$$

$$\sigma_{r\phi} = \sigma_{\theta\phi} = 0, \quad (13)$$

where P is the indenter load, B is the blister field strength, and ν is the Poisson's ratio; the origin of the spherical coordinate system lies on the surface at the contact point, θ is the angle to the loading axis, and ϕ is the angle around this axis as shown in Fig. 6.

Different cracks are driven by different components of the stress field around an indent. For example, ring, radial, lateral, and median cracks are driven by $\sigma_{rr}(\theta = \frac{\pi}{2})$, $\sigma_{\phi\phi}(\theta = \frac{\pi}{2})$, $\sigma_{rr}(\theta = 0)$, and $\sigma_{\theta\theta}(\theta = 0)$, respectively [48]. The magnitude of the blister field strength B controls the way glasses crack under load; glasses with a high blister field strength crack more readily than others [49,50]. According to the expanding cavity model, the volume shrinkage (densification) serves as an alternative to the plastic zone expansion under the indenter [51]. Therefore, deformation by densification is believed to produce less blister field stress and less subsurface damage, so the threshold load required to initiate cracks increases [47,49,51,52]. Cook and Pharr proposed that the blister field strength is proportional to $fE(P/H)^{3/2}$ during indentation, where P is the indenter load, E is the Young's modulus, H is hardness, and f is a parameter between 0 and 1, which accounts for the densification contribution in glass during indentation deformation [49]. $f = 0$ when the indentation volume is accommodated entirely by densification, and $f = 1$ when no densification occurs. Therefore, a lot of emphasis was placed on experimentally quantifying the contribution of densification using AFM in the literature as discussed in Sec. II. Furthermore, Sellappan *et al.* [50] provided an expression for calculating the blister field strength according to

$$B = \frac{3E}{4\pi(1+\nu)(1-2\nu)}(1 - V_R - V_P)V_i^-, \quad (14)$$

where V_i^- is the volume of indent before annealing, V_R is the volume recovery ratio, and V_P is the pileup ratio, calculated from AFM profiling of indents before and after sub-T_g annealing.

$$V_R = V_d/V_i^-, \quad (15)$$

$$V_P = (2V_i^+ - V_a^+)/V_i^-. \quad (16)$$

Volumes of permanent deformation through densification (V_d) and shear flow (V_s) can be calculated by

$$V_d = (V_i^- - V_a^-) + (V_a^+ - V_i^+). \quad (17)$$

$$V_s = V_i^- - V_d = V_i^+ + V_a^- - V_a^+, \quad (18)$$

where V_a^- is the volume of the indent after annealing; V_i^+ and V_a^+ are the pileup volumes before and after annealing, respectively [44]. Glass with a high V_R is expected to have a low blister field strength, a low residual stress, and therefore a low tendency to crack. While some studies found that crack resistance is correlated with V_R or the recovery of indentation depth (RID) [42], recent studies have contested this relationship by considering a large set of glasses [6,14]. Our AFM results in Table II also show that V_R could not satisfactorily explain the large variation in crack resistance of glasses that were considered in this study. Annealed 20% B_2O_3 glass has a higher V_R than as-drawn 20% B_2O_3 glass, but a lower crack resistance. Similarly, 10% B_2O_3 glass has a higher V_R than as-drawn 20% B_2O_3 glass, but also a lower crack resistance.

The above results and previous studies [5,14] suggest that there are other factors affecting the crack resistance of glasses besides densification and shear flow, which will be discussed in the following sections.

B. Deformation of boron-containing glasses: Network adaptivity and recovery

Figure 7 presents the longitudinal Brillouin frequency shift as a function of pressure during compression. Both as-drawn and annealed 20% B_2O_3 glasses were found to soften upon initial compression (a similar behavior is seen in 10% B_2O_3 glass, but to a lesser extent). As-drawn 20% B_2O_3 glass is softer at ambient conditions and up to ~3 GPa, then overlaps with the annealed 20% B_2O_3 sample. As-drawn 20% B_2O_3

TABLE II. Indent profiling using atomic force microscopy (AFM).

	V_i^- (μm^3)		V_i^+(μm^3)		V_a^- (μm^3)		V_a^+ (μm^3)		V_d (μm^3)		V_s (μm^3)		V_R	
	Avg	Std dev	Avg	Std dev	Avg	Std dev	Avg	Std dev	Avg	Std dev	Avg	Std dev	Avg	Std dev
As-drawn 20% B_2O_3	73.3	3.77	0.19	0.13	33.66	1.79	0.88	0.14	40.34	3.53	32.96	1.81	0.55	0.03
Annealed 20% B_2O_3	71.88	3.44	0.28	0.09	25.56	0.95	1.55	0.4	47.58	2.92	24.3	1.18	0.66	0.01
10% B_2O_3	71.75	1.67	0.08	0.04	27.58	1.05	0.97	0.45	45.06	1.12	26.69	1.14	0.63	0.01

glass elastically stiffens much faster than glasses with lower B_2O_3 content after passing the minimum around 2 GPa.

To better understand the crack resistance of boron-containing glasses, we measured their EOS, shown in Fig. 8. Below ~7 GPa, the volumes of all three boron-containing glasses decrease quickly with pressure, then as-drawn 20% B_2O_3 and 10% B_2O_3 glasses become more difficult to compress and approach the behavior of 0% B_2O_3 glass when the pressure is above 10 GPa. The smooth changes in density of all the glasses during compression in the low-pressure region suggest a gradual rearrangement of the glass structure with pressure that may involve small changes in the intermediate-range structure of the glass [53]. The sharp change in the ease of densification near 7 GPa in as-drawn 20% B_2O_3 and 10% B_2O_3 glasses may be related to some dramatic structural changes under pressure, such as conversion of boron atoms from the threefold to the fourfold coordination state. *In situ* neutron scattering [54] and inelastic x-ray scattering [55] studies on pure B_2O_3 glass showed that fourfold coordinated boron atoms begin to appear in appreciable amounts when pressure is greater than ~7 GPa. This coordination conversion in pure B_2O_3 glass was also observed in *in situ* BLS experiments in a DAC around ~7 GPa as a sharp increase in longitudinal sound velocity [56]. Figure 8 shows that upon initial compression, as-drawn 20% B_2O_3 and annealed 20% B_2O_3 glass behave similarly; the small difference may be related to differences in IRO as discussed in Sec. III A. On further increasing pressure, it can be seen from Fig. 8 that as-drawn 20% B_2O_3 glass seems to be more difficult to further compress. There is a slightly higher concentration of threefold boron in the as-drawn glass as compared to the annealed one as shown in Fig. 3(a). This means that the former would have a higher capacity to undergo structural changes and adapt to the higher load as compared to the latter, which is in agreement with the results in Fig. 8. The decrease in the slope of V/V_0 vs P for boron-containing glasses indicates the decreased compressibility of the high-pressure structure as compared to the low-pressure structure. Therefore the ability of a glass network to undergo significant structural changes during loading may be quantified from this change of slope. A higher ability of glass to undergo structural changes under pressure reflects its higher capacity to accommodate similar changes during indentation, dissipating energy, thus improving the damage resistance as a result.

The ability of glass to accommodate stress in the indentation process either through structural changes or through densification was earlier recognized as network adaptivity, and crack resistance was proposed to be correlated to network

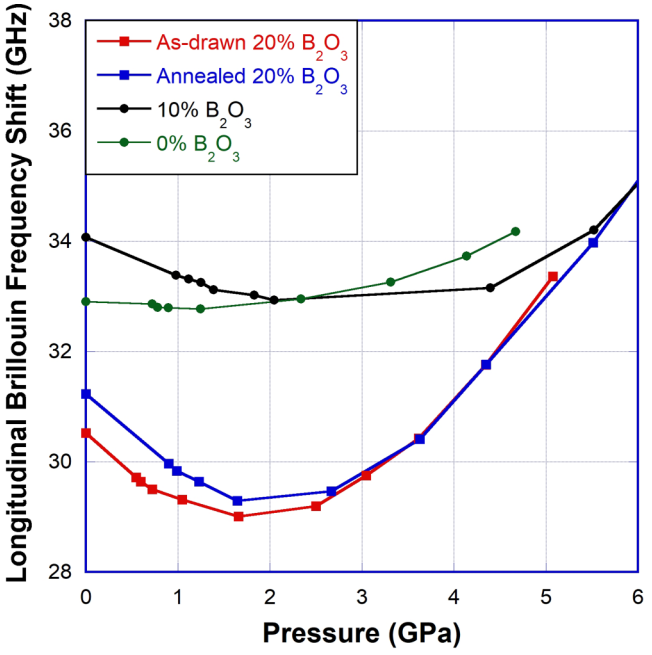

FIG. 7. Longitudinal Brillouin frequency shift as a function of pressure during compression for as-drawn and annealed 20% B_2O_3, and 10% and 0% B_2O_3 glasses.

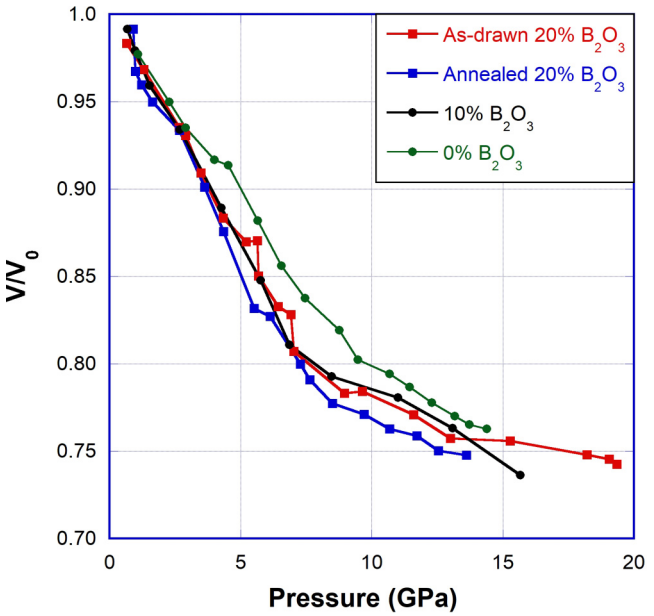

FIG. 8. EOS of as-drawn and annealed 20%, 10%, and 0% B_2O_3 glasses during compression.

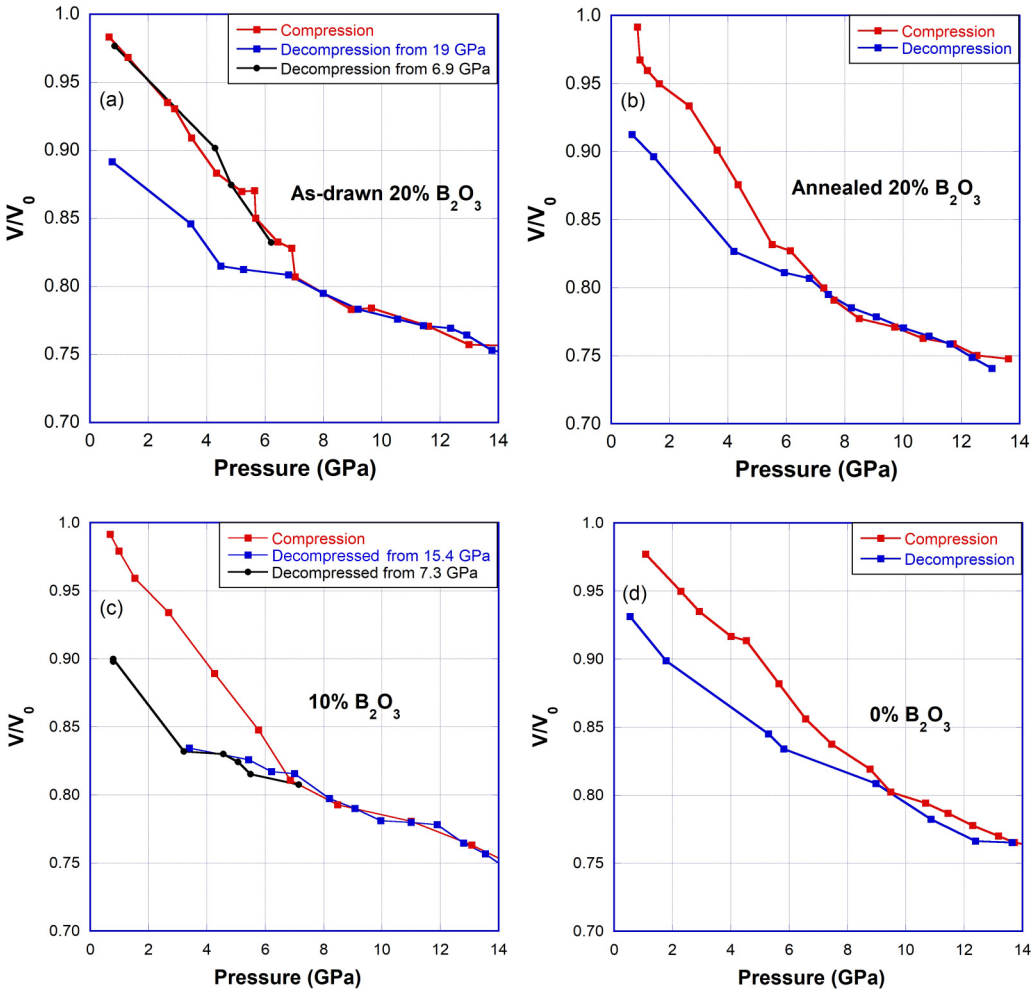

FIG. 9. EOS of (a) as-drawn 20% B_2O_3, (b) annealed 20% B_2O_3, (c) 10% B_2O_3, and (d) 0% B_2O_3 glasses during compression and decompression.

adaptivity [6]. However, the quantification of network adaptivity was based on changes in glass structure from hot compression [6], which may not necessarily reflect the structural changes at room temperature [19]. Methods to quantify the network adaptivity at room temperature are needed, which are more relevant to the indentation process. The slope change in the V/V_0 vs P curve shown in Fig. 8 may be considered as one of such methods, which needs to be confirmed by testing different glass systems.

Figure 9 shows the response of glasses to compression and the resulting recovery on decompression. Hydrostatically compressed glasses undergo elastic deformation initially; when pressure is increased further, they undergo plastic deformation [27]. On decompressing after the plastic deformation has occurred, initially the decompression curve traces the compression curve. On decompressing further, some of the changes are recovered but some of the changes become permanent. Boron-containing glasses undergo elastic deformation up to ∼7 GPa [see decompression from 6.9 GPa in Fig. 9(a)]; permanent changes occur upon decompression from higher pressures as seen in Figs. 9(a)–9(c). These glasses show a sharp change in V/V_0 vs P upon decompression around 3–4 GPa, which indicates that a significant part of the structural changes during compression are recovered on decompression below this pressure. Previous BLS measurements of pure B_2O_3 glass also showed that upon decompression, the longitudinal sound velocity decreases slowly first, then exhibits a large discontinuity at about 3 GPa [56], which was attributed to the boron coordination change from fourfold to threefold. Similar coordination conversion possibly occurs here in boron-containing glasses. Figure 9(d) shows that the volume decrease (thus densification) of 0% B_2O_3 glass is smaller compared to boron-containing glasses under the same pressure, and there is no sharp change in slope seen at ∼7 GPa. Upon decompression, volume is gradually recovered without dramatic change in slope at 3–4 GPa. Such detailed information gained through *in situ* measurements in DAC is not captured through postmortem analysis, such as the AFM profiling of indent before and after annealing.

Figure 10 shows the change of the longitudinal Brillouin frequency shift during compression and decompression of the annealed 20% B_2O_3 glass in comparison with that of silica glass [19]. Even though both glasses soften upon initial compression, the former gets stiffer under pressure much faster than the latter after passing through the minimum, which may be due to the change of boron coordination from 3 to 4 [54]. During decompression, the elastic property of the annealed 20% B_2O_3 glass decreases much faster than silica glass as

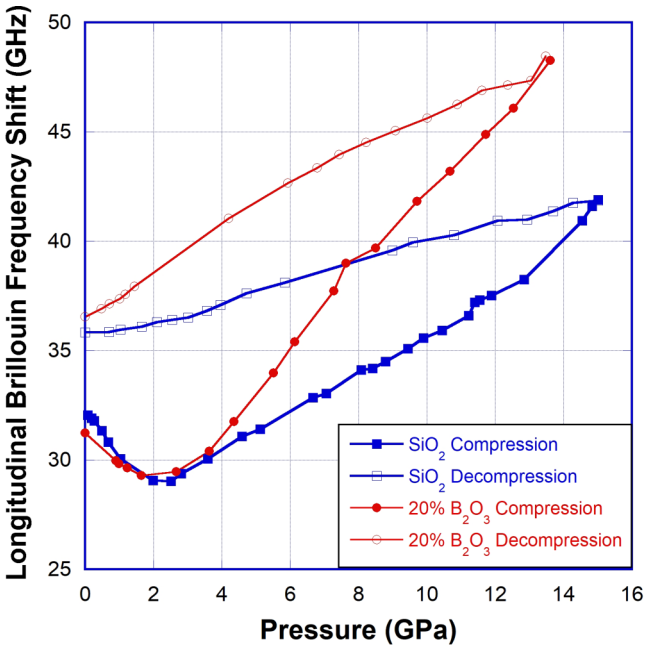

FIG. 10. Longitudinal Brillouin frequency shift in annealed 20% B_2O_3 glass and silica glass [19] as a function of pressure during compression (solid symbols) and decompression (open symbols).

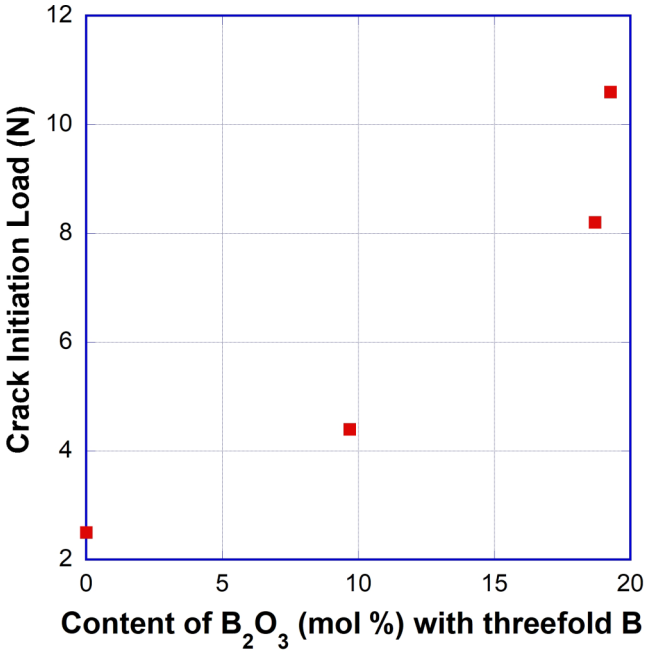

FIG. 11. Dependence of the crack initiation load on the content of trigonal boron.

well, indicating the possible recovering of boron coordination from 4 to 3, as observed in previous studies [54,56–58]. In the pressure range tested in Fig. 10, silicon is predominantly fourfold coordinated [59]. The densification of silica mainly occurs through the compaction in the IRO without coordination change in the SRO [60,61].

Figures 9 and 10 clearly show the different compression and decompression behaviors of glasses with and without boron. Different responses to loading and unloading during the indentation process would be expected in glasses with and without boron, which are hard to quantify during indentation, but inevitably lead to different stress/residual stress buildup, thus resulting in different crack resistance and cracking patterns. The "reversible" boron coordination change during loading and unloading helps increase the crack resistance of glass in at least three ways: (1) to dissipate energy; (2) to provide a highly compact coordination state for densification; (3) the coordination reversal during decompression acts like pseudoelasticity to reduce the residual stress buildup after unloading. This is reflected in Fig. 11, which shows a clear positive correlation between the crack initiation load and the content of trigonal boron in the glass structure.

Further evidence that coordination change at room temperature is mostly reversible can be found from *ex situ* structural studies on boron-containing glasses compressed at varying temperatures. Figure 12 presents NMR results from one such study on the 20% B_2O_3 glass where samples were pressure treated at 1 GPa for 1 h at different temperatures (different as-drawn glass samples were used for experimental results shown in Figs. 3(a) and 12, causing a slight difference in the calculated N_4 fraction). These results indicate that a substantial increase in fourfold coordinated boron is found with increasing temperature until 650 °C, but no significant permanent changes are seen after the compression-decompression cycle at room temperature (see the overlap of the blue and red spectra in Fig. 12). This implies that boron coordination change is largely reversible at room temperature, which lends support to our observations in the DAC. More detail on the experimental procedure used for preparing samples shown in Fig. 12 can be found elsewhere [62].

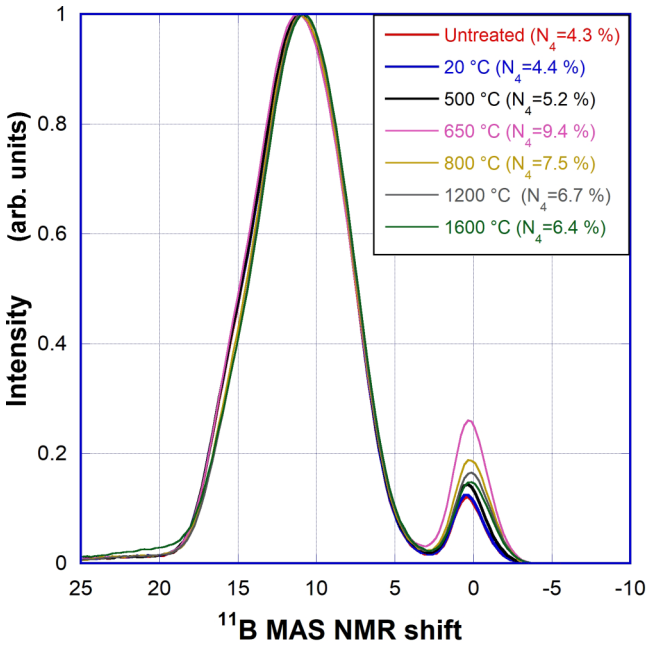

FIG. 12. Ambient ^{11}B MAS NMR spectra of 20% B_2O_3 glass compressed under 1 GPa for 1 h at varying temperatures indicated in legends.

C. Necessity for an improved description of blister field stress

In the expression for blister field stress given by Cook and Pharr, as discussed in Sec. III A, it was assumed that this stress remains constant during unloading, with the magnitude of B being equal to its value at the maximum load [49]. However, Bobji and Biswas later showed that the magnitude of B changes during unloading and depends on the recovery path that the material adopts when the indentation load is removed [63]. As discussed before, densification via intermediate-range structural changes or coordination conversion in the short range are non–volume conserving, whereas shear flow is volume conserving. The coordination conversion during loading and its reversal during unloading should be considered in the f parameter in order to calculate the blister field correctly, especially for boron-containing glasses. The difficulty is that the reversible coordination conversion during the loading and unloading cycle could leave no trace in post-mortem analysis such as AFM profiling of indents before and after sub-T_g annealing, or *ex situ* measurement of densification after hydrostatic compression and decompression process.

As seen in Table II, as-drawn 20% B_2O_3 glass has the lowest V_R, yet the highest crack initiation load. This is because its high content of trigonal boron provides a remarkable network adaptivity through reversible coordination conversion during the loading and unloading process. This means that the blister field strength or the residual stress around the indent imprint is very low after unloading, thus exhibiting a higher crack resistance. Previous studies on boron-containing glasses that considered the expression in Eq. (14) for calculating the blister field strength shared the same observation that glasses with the highest crack resistance do not exhibit the highest values of V_R [14]. This is because V_R may not reflect the true densification during loading and unloading in boron-containing glasses, indicating that the expression in Eq. (14) is insufficient to describe the blister field strength in such glass systems. These observations point towards the need to go beyond the simplified considerations of densification and shear flow alone to calculate residual stresses in complex glass systems. Our study showed that the reversible coordination conversion during loading and unloading should be considered for boron-containing glasses in order to understand their indentation and cracking behaviors. Attention should also be given to other species such as aluminum or germanium that can underdo coordination changes in the pressure range (up to ∼10 GPa) relevant to indentation experiments.

D. Perspective: Case for *in situ* studies to understand crack resistance

Cracks can develop during the loading or unloading process [49]. For glasses that undergo significant structural changes or density changes to accommodate stress on application of an external load, a major fraction of such changes may be reverted upon the release of the load, which cannot be captured by *ex situ* analysis of the indentation imprint left after unloading. For example, in the *ex situ* analysis of Yoshida *et al.* that was presented in Sec. III A, V_R is essentially the fraction of permanently densified volume to the total volume of the indent imprint [40]. V_R does not capture volume changes associated with reversible structural changes in terms of coordination conversion, and hence may not directly relate to the damage resistance of glass. The steep increase in densification and elastic property in response to compression and subsequent fast recovery during decompression seen in Figs. 9 and 10 for 20% B_2O_3 glass cannot be captured by *ex situ* analysis, but it is exactly this steep increase during compression and eventual recovery during decompression that reflects the structural adaptivity of the 20% B_2O_3 glass network, which in turn leads to its high damage resistance. Therefore, it is essential to develop *in situ* techniques that enable a fundamental understanding of the elastic as well as the plastic responses of glasses to sharp contact loading. Easy implementation and integration of various characterization techniques *in situ* in a DAC make it a valuable tool to obtain such information. At the same time, it is essential to extend such *in situ* techniques to indentation to understand the changes in local structure and properties of glasses in response to sharp contact loading.

IV. CONCLUSIONS

A few multicomponent glasses with vastly different indentation cracking behaviors and varying B_2O_3 contents were studied in a diamond anvil cell (DAC) by using integrated *in situ* optical microscopy and Brillouin light scattering techniques. These experiments provided the elastic and densification response of glasses to hydrostatic compression and decompression. As-drawn 20% and 10% B_2O_3 glasses show a sharp change in the ease of densification near 7 GPa, which may be related to structural changes such as conversion of boron atoms from the threefold to the fourfold coordination state. Interestingly, a large part of this change was found to be recovered on decompression, probably due to boron atoms reverting to the threefold coordination state. The ease of a glass network to undergo reversible structural changes in terms of coordination conversion during loading and unloading seems to be correlated with high crack resistance. This is due to the reduced stress buildup during loading and the reduced residual stress after unloading, thus decreasing the driving force for cracking.

ACKNOWLEDGMENTS

This work was supported by the National Science Foundation under Grants No. DMR-1508410 and No. 1255378. Yue Zhai's help with indentation experiments is very much appreciated.

[1] A. J. Ellison, J. S. Frackenpohl, J. C. Mauro, D. M. Noni, Jr., and N. Venkataraman, US Patent No. 0,291,845 A1 (October 2017).

[2] L. Wondraczek, J. C. Mauro, J. Eckert, U. Kühn, J. Horbach, J. Deubener, and T. Rouxel, Adv. Mater. **23**, 4578 (2011).

[3] J. Luo, P. J. Lezzi, K. D. Vargheese, A. Tandia, J. T. Harris, T. M. Gross, and J. C. Mauro, Front. Mater. **3**, 52 (2016).

[4] K. G. Aakermann, K. Januchta, J. A. L. Pedersen, M. N. Svenson, S. J. Rzoska, M. Bockowski, J. C. Mauro, M. Guerette, L. Huang, and M. M. Smedskjaer, J. Non-Cryst. Solids **426**, 175 (2015).

[5] K. Januchta, R. E. Youngman, A. Goel, M. Bauchy, S. J. Rzoska, M. Bockowski, and M. M. Smedskjaer, J. Non-Cryst. Solids **460**, 54 (2017).

[6] K. Januchta, R. E. Youngman, A. Goel, M. Bauchy, S. L. Logunov, S. J. Rzoska, M. Bockowski, L. R. Jensen, and M. M. Smedskjaer, Chem. Mater. **29**, 5865 (2017).

[7] K. Januchta, M. Bauchy, R. E. Youngman, S. J. Rzoska, M. Bockowski, and M. M. Smedskjaer, Phys. Rev. Mater. **1**, 063603 (2017).

[8] G. Scannell, L. Huang, and T. Rouxel, J. Non-Cryst. Solids **429**, 129 (2015).

[9] J. Luo, K. D. Vargheese, A. Tandia, J. T. Harris, and J. C. Mauro, J. Non-Cryst. Solids **452**, 297 (2016).

[10] J. Sehgal and S. Ito, J. Am. Ceram. Soc. **81**, 2485 (1998).

[11] T. M. Gross, M. Tomozawa, and A. Koike, J. Non-Cryst. Solids **355**, 563 (2009).

[12] P. Malchow, K. E. Johanns, D. Möncke, S. Korte-Kerzel, L. Wondraczek, and K. Durst, J. Non-Cryst. Solids **419**, 97 (2015).

[13] C. Zehnder, S. Bruns, J.-N. Peltzer, K. Durst, S. Korte-Kerzel, and D. Möncke, Front. Mater. **4**, 5 (2017).

[14] R. Limbach, A. Winterstein-Beckmann, J. Dellith, D. Möncke, and L. Wondraczek, J. Non-Cryst. Solids **417**, 15 (2015).

[15] M. J. Dejneka, J. C. Mauro, M. Potuzak, M. M. Smedskjaer, and R. E. Youngman, US Patent No. 9,145,333 B1 (September 2015).

[16] T. Rouxel, H. Ji, J. P. Guin, F. Augereau, and B. Rufflé, J. Appl. Phys. **107**, 94903 (2010).

[17] J. C. Mauro, A. Tandia, K. D. Vargheese, Y. Z. Mauro, and M. M. Smedskjaer, Chem. Mater. **28**, 4267 (2016).

[18] T. Rouxel, H. Ji, T. Hammouda, and A. Moréac, Phys. Rev. Lett. **100**, 225501 (2008).

[19] M. Guerette, M. R. Ackerson, J. Thomas, F. Yuan, E. Bruce Watson, D. Walker, and L. Huang, Sci. Rep. **5**, 15343 (2015).

[20] C. Meade and R. Jeanloz, Phys. Rev. B **35**, 236 (1987).

[21] T. Sato and N. Funamori, Phys. Rev. Lett. **101**, 255502 (2008).

[22] O. B. Tsiok, V. V. Brazhkin, A. G. Lyapin, and L. G. Khvostantsev, Phys. Rev. Lett. **80**, 999 (1998).

[23] J. Schroeder, T. G. Bilodeau, and X.-S. Zhao, High Pressure Sci. Technol. **4**, 531 (1990).

[24] D. Wakabayashi, N. Funamori, T. Sato, and T. Taniguchi, Phys. Rev. B **84**, 144103 (2011).

[25] K. H. Smith, E. Shero, A. Chizmeshya, and G. H. Wolf, J. Chem. Phys. **102**, 6851 (1995).

[26] S. Sundararaman, W.-Y. Ching, and L. Huang, J. Non-Cryst. Solids **445**, 102 (2016).

[27] T. J. Holmquist and G. R. Johnson, J. Appl. Mech. **78**, 51003 (2011).

[28] J. C. Mauro, D. C. Allan, and M. Potuzak, Phys. Rev. B **80**, 094204 (2009).

[29] R. C. Welch, J. R. Smith, M. Potuzak, X. Guo, B. F. Bowden, T. J. Kiczenski, D. C. Allan, E. A. King, A. J. Ellison, and J. C. Mauro, Phys. Rev. Lett. **110**, 265901 (2013).

[30] M. Guerette and L. Huang, J. Phys. D: Appl. Phys. **45**, 275302 (2012).

[31] S. P. Jaccani and L. Huang, Int. J. Appl. Glass Sci. **7**, 452 (2016).

[32] S. P. Jaccani, S. Sundararaman, and L. Huang, J. Am. Ceram. Soc. **102**, 1137 (2019).

[33] F. Datchi, A. Dewaele, P. Loubeyre, R. Letoullec, Y. Le Godec, and B. Canny, High Pressure Res. **27**, 447 (2007).

[34] S. Klotz, J. C. Chervin, P. Munsch, and G. Le Marchand, J. Phys. D: Appl. Phys. **42**, 75413 (2009).

[35] J. C. Chervin, B. Canny, and M. Mancinelli, High Pressure Res. **21**, 305 (2001).

[36] D. Nečas and P. Klapetek, Open Phys. **10**, 181 (2012).

[37] T. Sato, N. Funamori, and T. Yagi, Nat. Commun. **2**, 345 (2011).

[38] C. Sonneville, A. Mermet, B. Champagnon, C. Martinet, J. Margueritat, D. De Ligny, T. Deschamps, and F. Balima, J. Chem. Phys. **137**, 124505 (2012).

[39] S. A. Amin, E. N. Rissi, K. McKiernan, and J. L. Yarger, Rev. Sci. Instrum. **83**, 33702 (2012).

[40] S. Yoshida, J.-C. Sanglebœuf, and T. Rouxel, J. Mater. Res. **20**, 3404 (2005).

[41] J. Sehgal and S. Ito, J. Non-Cryst. Solids **253**, 126 (1999).

[42] Y. Kato, H. Yamazaki, S. Yoshida, and J. Matsuoka, J. Non-Cryst. Solids **356**, 1768 (2010).

[43] B. R. Lawn and D. B. Marshall, J. Am. Ceram. Soc. **62**, 347 (1979).

[44] G. W. Scannell, D. Laille, F. Célarié, L. Huang, and T. Rouxel, Front. Mater. **4**, 6 (2017).

[45] Y. Shi, J. Luo, F. Yuan, and L. Huang, J. Appl. Phys. **115**, 43528 (2014).

[46] J. J. Lewandowski, W. H. Wang, and A. L. Greer, Philos. Mag. Lett. **85**, 77 (2005).

[47] E. H. Yoffe, Philos. Mag. A **46**, 617 (1982).

[48] T. Rouxel, Philos. Trans. R. Soc., A **373**, 20140140 (2015).

[49] R. F. Cook and G. M. Pharr, J. Am. Ceram. Soc. **73**, 787 (1990).

[50] P. Sellappan, T. Rouxel, F. Celarie, E. Becker, P. Houizot, and R. Conradt, Acta Mater. **61**, 5949 (2013).

[51] S. S. Chiang, D. B. Marshall, and A. G. Evans, J. Appl. Phys. **53**, 298 (1982).

[52] B. Lawn, *Fracture of Brittle Solids* (Cambridge University Press, Cambridge, 1993).

[53] J. Nicholas, S. Sinogeikin, J. Kieffer, and J. Bass, J. Non-Cryst. Solids **349**, 30 (2004).

[54] A. Zeidler, K. Wezka, D. A. Whittaker, P. S. Salmon, A. Baroni, S. Klotz, H. E. Fischer, M. C. Wilding, C. L. Bull, M. G. Tucker, M. Salanne, G. Ferlat, and M. Micoulaut, Phys. Rev. B **90**, 024206 (2014).

[55] S. K. Lee, P. J. Eng, H. Mao, Y. Meng, M. Newville, M. Y. Hu, and J. Shu, Nat. Mater. **4**, 851 (2005).

[56] J. Nicholas, S. Sinogeikin, J. Kieffer, and J. Bass, Phys. Rev. Lett. **92**, 215701 (2004).

[57] L. Huang, J. Nicholas, J. Kieffer, and J. Bass, J. Phys.: Condens. Matter **20**, 75107 (2008).

[58] D. A. Kilymis, J.-M. Delaye, and S. Ispas, J. Chem. Phys. **143**, 94503 (2015).

[59] P. S. Salmon and A. Zeidler, J. Phys.: Condens. Matter **27**, 133201 (2015).

[60] L. Huang and J. Kieffer, Phys. Rev. B **69**, 224203 (2004).

[61] L. Huang and J. Kieffer, Phys. Rev. B **69**, 224204 (2004).

[62] M. M. Smedskjaer, S. J. Rzoska, M. Bockowski, and J. C. Mauro, J. Chem. Phys. **140**, 54511 (2014).

[63] M. S. Bobji and S. K. Biswas, Philos. Mag. A **73**, 399 (1996).